Journal of Sound and Vibration 329 (2010) 3647–3659

Contents lists available at ScienceDirect

Journal of Sound and Vibration

journal homepage: www.elsevier.com/locate/jsvi

Distributed shell control with a new multi-DOF photostrictive actuator design

H.H. Yue [a], G.L. Sun [a], Z.Q. Deng [a], H.S. Tzou [a,b,*]

[a] School of Mechatronic Engineering, Harbin Institute of Technology, Harbin 150001, China
[b] Department of Mechanical Engineering, StrucTronics Lab, University of Kentucky, Lexington, KY 40506-0503, USA

ARTICLE INFO

Article history:
Received 18 April 2009
Received in revised form
7 January 2010
Accepted 11 March 2010
Handling Editor: D.J. Wagg
Available online 24 April 2010

ABSTRACT

With the photovoltaic effect and the converse piezoelectric effect, the lanthanum-modified lead zirconate titanate (PLZT) actuator can transform the narrow-band photonic energy to mechanical strain/stress—the *photodeformation effect*. This photodeformation process can be further used for non-contact precision actuation and control in various structural, biomedical and electromechanical systems. Although there are a number of design configurations of distributed actuators, e.g., segmentation and shaping, been investigated over the years, this study is to explore a new actuator configuration spatially bonded on the surface of shell structures to enhance the spatial modal controllability. A mathematical model of a new multiple degree-of-freedom (multi-DOF) photostrictive actuator configuration is presented first, followed by the photostrictive/shell coupling equations of a cylindrical shell structure laminated with the newly proposed multi-DOF distributed actuator. Distributed microscopic photostrictive actuation and its contributing components of a one-piece actuator and the multi-DOF actuator are evaluated in the modal domain. Effects of shell's curvature and actuator's size are also evaluated. Parametric analyses suggest that the new multi-DOF distributed actuator, indeed, provides better performance and control effect to shell actuation and control. This multi-DOF configuration can be further applied to actuation and control of various shell and non-shell structures.

1. Introduction

Smart structures and structronic systems with distributed sensors and actuators have been extensively studied and evaluated over the last two decades [1–3]. Distributed actuators designed by various smart materials, such as piezoelectric, shape memory alloy, electro-/magneto-strictive, etc. materials, have been widely applied to control of static shapes and dynamic oscillations of flexible structures. However, these conventional "smart" actuators require hard-wire connections to transmit energy sources and control commands. To avoid electrical noises influenced by cross talks and/or electrical or magnetic fields, a wireless non-contact photostrictive actuator system has been proposed [4–7] and the $(Pb,La)(Zr,Ti)O_3$ ceramic doped with WO_3 (PLZT) is emerging as a new type of photostrictive actuation material. With the photovoltaic effect and the converse piezoelectric effect, the PLZT photostrictive actuator uses photonic energy, instead of electric or magnetic energy, to induce mechanical strain or stress. Due to its unique non-contact actuation characteristic, one-dimensional (1D) photostrictive actuators have been studied over the years [8–13]. Two-dimensional (2D)

* Corresponding author. Current address: School of Aeronautics and Astronautics, Zhejiang University, Hangzhou 310027, China. Tel.: +1 859 257 6336x80643; fax: +1 859 257 3304.
E-mail addresses: hstzou@engr.uky.edu, hstzou@zju.edu.cn (H.S. Tzou).

0022-460X/$ - see front matter © 2010 Elsevier Ltd. All rights reserved.
doi:10.1016/j.jsv.2010.03.016

photostrictive actuators applied to plate control were also investigated [14,15]. Distributed 1D and 2D photostrictive actuators applied to actuation and control of cylindrical shells and parabolic shells have been investigated recently [16–19]. Although a number of design configurations have been evaluated (i.e., segmentation and shaping), new effective actuator design configurations for multi-mode dynamic control of shell structures needs to be further explored.

Earlier studies revealed actuation deficiencies of distributed structures, e.g., modal filtering or ineffective to certain structural modes, when a single one-piece actuator was applied to distributed structures [17,20]. In this study, a new multiple degree-of-freedom (multi-DOF) distributed photostrictive actuator is proposed and its multiple modal control actions on cylindrical shells are evaluated. A mathematical model of the multi-DOF photostrictive actuator is presented first, followed by the photostrictive/shell coupling equations of a cylindrical shell laminated with a center-located multi-DOF actuator. Spatial modal actuations of a conventional one-piece actuator and the new multi-DOF actuator are evaluated and compared. Effects of actuator sizes (defined by the actuator and shell dimension ratios) and the control actions of actuator on the variable-curvature shells (with constant shell size) are investigated.

2. 1D photostrictive actuation

An unconstrained one-dimensional (1D) PLZT photostrictive actuator (with dimensions of $L^a \times b^a \times h^a$) is shown in Fig. 1. It is polarized in the α_1-direction and the two electrodes are on the α_2–α_3 end surfaces separated by the actuator length L^a. The actuator exhibits *a photodeformation effect* which involves two fundamental effects: the *photovoltaic effect* and the *converse piezoelectric effect*. A specified narrowband light irradiated on the optical actuator first induces a photovoltaic current which generates a voltage between the two surface electrodes, and this phenomenon is known as the photovoltaic effect. Based on the converse piezoelectric effect, the photovoltaic voltage induces a uniform extensional strain along the polarization direction of the PLZT actuator, as shown in Fig. 1. Formulation of the distributed control effect resulting from the photodeformation is presented next.

As discussed above, the photodeformation effect involves two stages, i.e., the photovoltaic effect and the converse piezoelectric effect. The light induced photovoltaic voltage $E_l(t)$ in an incremental form is [15]

$$E_l(t_j) = E_l(t_{j-1}) + \left\{ [E_s - E_l(t_{j-1})] \frac{\alpha}{a_s} I(t_j) e^{-\alpha/a_s I(t_j)\Delta t} - E_l(t_{j-1}) \beta e^{-\beta \Delta t} \right\} \Delta t, \tag{1}$$

where E_s is the saturated photovoltaic voltage; t_j is the j-th time instant; a_s is the aspect ratio of length and width ($a_s = L^a/b^a$); $I(t_j)$ is the light intensity at time t_j; Δt is the time step; β is the voltage leakage constant; and α is the optical actuator constant. Then, this photovoltaic voltage induces a strain in the actuator, due to the converse piezoelectric effect. Furthermore, the high-energy light also heats up the actuator with the temperature response $\theta(t)$ as

$$\theta(t_j) = \theta(t_{j-1}) + \{[I(t_j)P - \gamma\theta(t_{j-1})]\Delta t\}/(H + \gamma \Delta t), \tag{2}$$

where P is the power of absorbed heat; H is the heat capacity of the optical actuator; and γ is the heat transfer rate. While the body temperature rises, the pyroelectric effect can lead to an additional electric voltage $E_\theta(t)$, which further enhances the strain, due to the converse piezoelectric effect.

$$E_\theta(t) = \frac{P_n}{\varepsilon} \theta(t), \tag{3}$$

where P_n is the pyroelectric constant; ε is the permittivity. Besides, since the high-energy light induces thermal effect, which reduces the spontaneous polarization and then the actuator control effect. Thus, the total induced strain and the resultant stress of the photostrictive actuator become

$$\overline{S}(t) = d_{33}[E_l(t) + E_\theta(t)] - \lambda\theta(t)/Y_a, \tag{4a}$$

$$\overline{T}(t) = Y_a d_{33}[E_l(t) + E_\theta(t)] - \lambda\theta(t), \tag{4b}$$

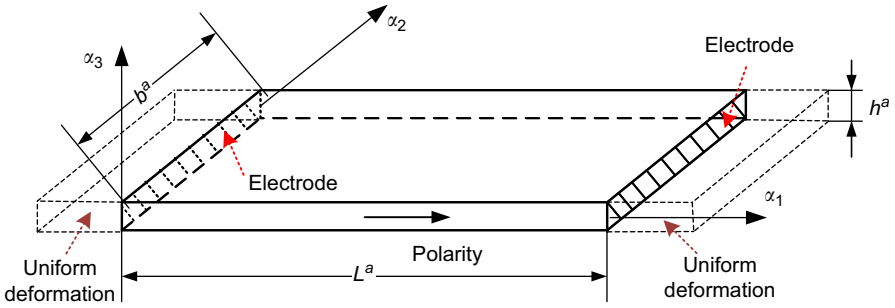

Fig. 1. Free-body diagram of 1D unconstrained photostrictive actuator.

where d_{33} is the piezoelectric strain constant; λ is the thermal stress coefficient; and Y_a is Young's modulus of the photostrictive actuator. Accordingly, the induced actuation force per unit width in the α_1-direction is

$$N_{11}^a(t) = h^a[Y_a d_{33}[E_l(t)+E_\theta(t)]-\lambda\theta(t)]. \tag{5}$$

3. Multi-DOF actuation

The proposed new multi-DOF actuator system consists of four regions or segments, Fig. 2(a), in which each region is made of a single-piece mono-axially sensitive photostrictive material with a pair of end electrodes, Fig. 1. Among the four regions and their paired electrodes, one end electrode of each region is fixed to a stable non-conducting cross fixture located in the middle of the four regions, while the other three sides are free to move. Thus, each photostrictive segment is acting like a "cantilever beam actuator" to the host structure. When activated by applying a high-intensity light, each region will induce uniform deformation as shown in Fig. 2(b). Unlike the conventional single one-piece actuator, this new design can induce four individual control actions independently or coordinately applied to structural control of plates and shells. Fig. 2(a) also illustrates the control forces induced in the four regions of the multi-DOF actuator design.

Now assume a curved multi-DOF actuator is applied to a cylindrical shell defined by (x,ψ,α_3). Here x, ψ and α_3 denote the longitudinal, circumferential, and transverse directions, respectively. Fig. 3 shows the cylindrical shell with the multi-DOF actuator with the coordinates marking the four regions of the multi-DOF actuator.

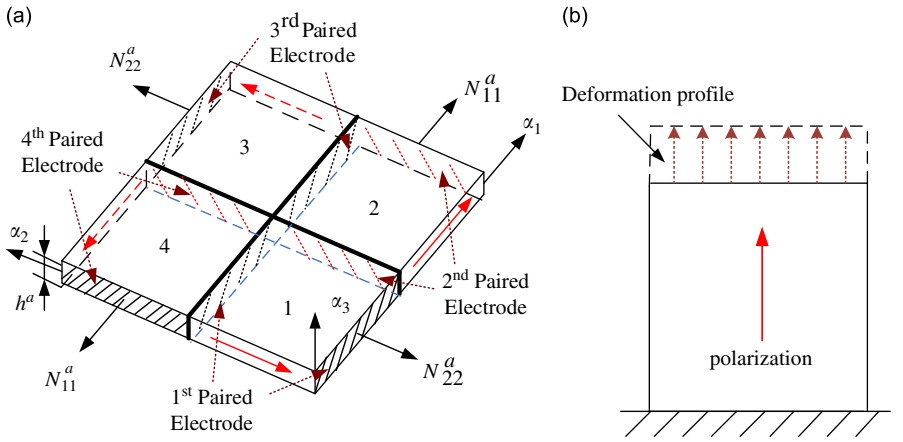

Fig. 2. Free-body diagram of the multi-DOF actuator (a) and uniform actuation (b).

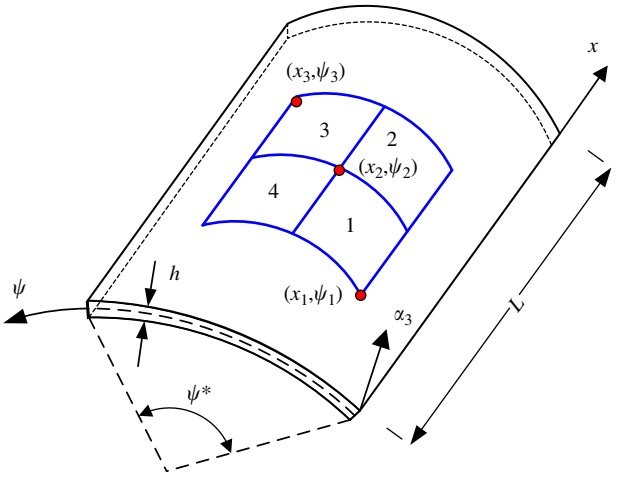

Fig. 3. A shell attached with the multi-DOF actuator.

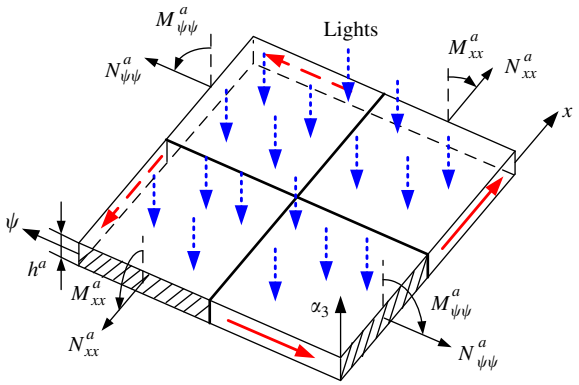

Fig. 4. The multi-DOF actuator induced control forces/moments to the shell structure.

The multi-DOF actuator under a high-energy light can introduce in-plane membrane control forces which, multiplied by their respective moment arms, can also result in control moments to the shell structure. (Note that the moment arm is the distance from the shell's neutral surface to the mid-surface of the actuator.) Fig. 4 shows the actuator generated control forces and moments to the shell structure. The induced membrane control forces and the bending control moments are defined next, followed by shell's system equations.

The control forces and moments (i.e., N_{ii}^a and M_{ii}^a) generated by the multi-DOF actuator are defined by their respective regions and coordinates.

$$N_{xx}^a = \begin{cases} h^a Y_a \bar{S}, & x_2 \le x \le x_3, \quad \psi_1 \le \psi \le \psi_2; \ x_1 \le x \le x_2, \ \psi_2 \le \psi \le \psi_3, \\ 0 & \text{elsewhere,} \end{cases} \tag{6a}$$

or

$$N_{xx}^a = \begin{cases} h^a Y_a \bar{S}[u_s(x-x_2) - u_s(x-x_3)] \times [u_s(\psi-\psi_1) - u_s(\psi-\psi_2)], \\ h^a Y_a \bar{S}[u_s(x-x_2) - u_s(x-x_1)] \times [u_s(\psi-\psi_3) - u_s(\psi-\psi_2)], \end{cases} \tag{6b}$$

$$N_{\psi\psi}^a = \begin{cases} h^a Y_a \bar{S}, & x_1 \le x \le x_2, \quad \psi_1 \le \psi \le \psi_2; \ x_2 \le x \le x_3, \ \psi_2 \le \psi \le \psi_3, \\ 0 & \text{elsewhere,} \end{cases} \tag{7a}$$

or

$$N_{\psi\psi}^a = \begin{cases} h^a Y_a \bar{S}[u_s(x-x_2) - u_s(x-x_3)] \times [u_s(\psi-\psi_2) - u_s(\psi-\psi_3)], \\ h^a Y_a \bar{S}[u_s(x-x_2) - u_s(x-x_1)] \times [u_s(\psi-\psi_2) - u_s(\psi-\psi_1)], \end{cases} \tag{7b}$$

$$M_{xx}^a = \begin{cases} \dfrac{h+h^a}{2} h^a Y_a \bar{S}, & x_2 \le x \le x_3, \quad \psi_1 \le \psi \le \psi_2; \ x_1 \le x \le x_2, \ \psi_2 \le \psi \le \psi_3, \\ 0 & \text{elsewhere,} \end{cases} \tag{8a}$$

or

$$M_{xx}^a = \begin{cases} \dfrac{h+h^a}{2} h^a Y_a \bar{S}[u_s(x-x_2) - u_s(x-x_3)] \times [u_s(\psi-\psi_1) - u_s(\psi-\psi_2)], \\ \dfrac{h+h^a}{2} h^a Y_a \bar{S}[u_s(x-x_2) - u_s(x-x_1)] \times [u_s(\psi-\psi_3) - u_s(\psi-\psi_2)], \end{cases} \tag{8b}$$

$$M_{\psi\psi}^a = \begin{cases} \dfrac{h+h^a}{2} h^a Y_a \bar{S}, & x_1 \le x \le x_2, \quad \psi_1 \le \psi \le \psi_2; \ x_2 \le x \le x_3, \ \psi_2 \le \psi \le \psi_3, \\ 0 & \text{elsewhere,} \end{cases} \tag{9a}$$

or

$$M_{\psi\psi}^a = \begin{cases} \dfrac{h+h^a}{2} h^a Y_a \bar{S}[u_s(x-x_2) - u_s(x-x_3)] \times [u_s(\psi-\psi_2) - u_s(\psi-\psi_3)], \\ \dfrac{h+h^a}{2} h^a Y_a \bar{S}[u_s(x-x_2) - u_s(x-x_1)] \times [u_s(\psi-\psi_2) - u_s(\psi-\psi_1)]. \end{cases} \tag{9b}$$

The longitudinal, circumferential and transverse governing equations of the shell with the multi-DOF photostrictive actuator can be derived as

$$-\frac{\partial N_{xx}}{\partial x}-\frac{1}{R}\frac{\partial N_{x\psi}}{\partial \psi}+\rho h\ddot{u}_x=\frac{\partial N^a_{xx}}{\partial x}; \tag{10}$$

$$-\frac{\partial N_{x\psi}}{\partial x}-\frac{1}{R}\frac{N_{\psi\psi}}{\partial \psi}-\frac{1}{R}\frac{\partial M_{x\psi}}{\partial x}-\frac{1}{R^2}\frac{\partial M_{\psi\psi}}{\partial \psi}+\rho h\ddot{u}_\psi=\frac{1}{R}\frac{\partial N^a_{\psi\psi}}{\partial \psi}+\frac{1}{R^2}\frac{\partial M^a_{\psi\psi}}{\partial \psi}; \tag{11}$$

$$-\frac{\partial^2 M_{xx}}{\partial x^2}-\frac{2}{R}\frac{\partial^2 M_{x\psi}}{\partial x\,\partial \psi}-\frac{1}{R^2}\frac{\partial^2 M_{\psi\psi}}{\partial \psi^2}+\frac{N_{\psi\psi}}{R}+\rho h\ddot{u}_3=\frac{\partial^2 M^a_{xx}}{\partial x^2}-\frac{N^a_{\psi\psi}}{R}+\frac{1}{R^2}\frac{\partial^2 M^a_{\psi\psi}}{\partial \psi^2}; \tag{12}$$

where N_{ij} and M_{ij} are the "elastic" forces and moments of the shell (i=x, and j=ψ); the superscript "a" denotes the control forces and moments generated by the photostrictive actuator. R is the shell radius; ρ is the shell density; h is the shell thickness; and $\ddot{u}_i$ is the acceleration. The left-side terms are related to shell's intrinsic elastic characteristics and the right-side terms are the photostrictive induced control forces and moments. Distributed actuation and its contributing control actions to cylindrical shells are analyzed next.

4. Independent modal control

It is assumed that the shell is simply supported on all four edges. Based on the modal expansion technique, the dynamic response of the shell can be represented by a sum of the response of all participating modes, i.e.,

$$u_i(x,\psi,t)=\sum_{m=1}^{\infty}\sum_{n=1}^{\infty}\eta_{imn}(t)U_{imn}(x,\psi)\quad \text{where } i=x,\psi,\alpha_3, \tag{13}$$

where U_{imn} is the mn-th or (m,n)th mode shape function and η_{imn} is the modal participation factor. Assume the transverse vibration dominates the shell oscillations and the transverse mode shape function of a simply supported shell is

$$U_{mn}=\sin(m\pi x/L)\sin(n\pi\psi/\psi^*), \tag{14}$$

where L and ψ^* are respectively the length and the curvature angle of the cylindrical shell. Substituting the modal expansion into the system equation and imposing the modal orthogonality yields the mn-th transverse modal equation of the cylindrical shell.

$$\ddot{\eta}_{mn}+2\xi_{mn}\omega_{mn}\dot{\eta}_{mn}+\omega^2_{mn}\eta_{mn}=F^c_{mn}, \tag{15}$$

where the modal control force is

$$F^c_{mn}=\frac{4}{\rho hLR\psi^*}\int_0^L\int_0^{\psi^*}\left(\frac{\partial^2 M^a_{xx}}{\partial x^2}-\frac{N^a_{\psi\psi}}{R}+\frac{1}{R^2}\frac{\partial^2 M^a_{\psi\psi}}{\partial \psi^2}\right)U_{mn}(x,\psi)\,R\,\mathrm{d}x\,\mathrm{d}\psi. \tag{16}$$

Integrating and simplifying each term in Eq. (16), respectively, yields three contributing actuation components:

$$\begin{aligned}\frac{4}{\rho hLR\psi^*}\int_0^L\int_0^{\psi^*}\frac{\partial^2 M^a_{xx}}{\partial x^2}U_{mn}(x,\psi)\,R\,\mathrm{d}x\,\mathrm{d}\psi&=\frac{2(h+h^a)h^a}{\rho hLR\psi^*}Y_a\bar{S}\int_0^L\int_0^{\psi^*}\frac{\partial^2}{\partial x^2}\{[u_s(x-x_2)-u_s(x-x_3)]\\&\times[u_s(\psi-\psi_1)-u_s(\psi-\psi_2)]+[u_s(x-x_2)-u_s(x-x_1)]\times[u_s(\psi-\psi_3)-u_s(\psi-\psi_2)]\}U_{mn}(x,\psi)\,R\,\mathrm{d}x\,\mathrm{d}\psi\\&=-\frac{2(h+h^a)h^a}{\rho hL\psi^*}Y_a\bar{S}\frac{m\psi^*}{nL}\left[\left(\cos\frac{m\pi x_2}{L}-\cos\frac{m\pi x_3}{L}\right)\times\left(\cos\frac{n\pi\psi_1}{\psi^*}-\cos\frac{n\pi\psi_2}{\psi^*}\right)\right.\\&\left.+\left(\cos\frac{m\pi x_2}{L}-\cos\frac{m\pi x_1}{L}\right)\times\left(\cos\frac{n\pi\psi_3}{\psi^*}-\cos\frac{n\pi\psi_2}{\psi^*}\right)\right]=-\tilde{M}_{xmn}\bar{S};\end{aligned} \tag{17a}$$

$$\begin{aligned}&\frac{4}{\rho hLR\psi^*}\int_0^L\int_0^{\psi^*}\frac{N^a_{\psi\psi}}{R}U_{mn}(x,\psi)\,R\,\mathrm{d}x\,\mathrm{d}\psi=\frac{4h^a}{\rho hLR^2\psi^*}Y_a\bar{S}\int_0^L\int_0^{\psi^*}\{[u_s(x-x_2)-u_s(x-x_3)]\times[u_s(\psi-\psi_2)-u_s(\psi-\psi_3)]\\&+[u_s(x-x_2)-u_s(x-x_1)]\times[u_s(\psi-\psi_2)-u_s(\psi-\psi_1)]\}U_{mn}(x,\psi)\,R\,\mathrm{d}x\,\mathrm{d}\psi=\frac{4h^a}{\rho hLR\psi^*}Y_a\bar{S}\frac{L\psi^*}{mn\pi^2}\left[\left(\cos\frac{m\pi x_2}{L}-\cos\frac{m\pi x_3}{L}\right)\right.\\&\left.\times\left(\cos\frac{n\pi\psi_2}{\psi^*}-\cos\frac{n\pi\psi_3}{\psi^*}\right)+\left(\cos\frac{m\pi x_2}{L}-\cos\frac{m\pi x_1}{L}\right)\times\left(\cos\frac{n\pi\psi_2}{\psi^*}-\cos\frac{n\pi\psi_1}{\psi^*}\right)\right]=\tilde{N}_{\psi mn}\bar{S};\end{aligned} \tag{17b}$$

$$\begin{aligned}\frac{4}{\rho hLR\psi^*}\int_0^L\int_0^{\psi^*}\frac{1}{R^2}\frac{\partial^2 M^a_{\psi\psi}}{\partial \psi^2}U_{mn}(x,\psi)\,R\,\mathrm{d}x\,\mathrm{d}\psi&=\frac{2(h+h^a)h^a}{\rho hLR^3\psi^*}Y_a\bar{S}\int_0^L\int_0^{\psi^*}\frac{\partial^2}{\partial \psi^2}\{[u_s(x-x_2)-u_s(x-x_3)]\times[u_s(\psi-\psi_2)\\&-u_s(\psi-\psi_3)]+[u_s(x-x_2)-u_s(x-x_1)]\times[u_s(\psi-\psi_2)-u_s(\psi-\psi_1)]\}U_{mn}(x,\psi)\,R\,\mathrm{d}x\,\mathrm{d}\psi\\&=\frac{-2(h+h^a)h^a}{\rho hLR^2\psi^*}Y_a\bar{S}\frac{nL}{m\psi^*}\left[\left(\cos\frac{m\pi x_2}{L}-\cos\frac{m\pi x_3}{L}\right)\times\left(\cos\frac{n\pi\psi_2}{\psi^*}-\cos\frac{n\pi\psi_3}{\psi^*}\right)\right.\\&\left.+\left(\cos\frac{m\pi x_2}{L}-\cos\frac{m\pi x_1}{L}\right)\times\left(\cos\frac{n\pi\psi_2}{\psi^*}-\cos\frac{n\pi\psi_1}{\psi^*}\right)\right]=-\tilde{M}_{\psi mn}\bar{S}.\end{aligned} \tag{17c}$$

Note that $\tilde{M}_{xmn}$, $\tilde{N}_{\psi mn}$ and $\tilde{M}_{\psi mn}$ include all effects contributed by actuator locations, shell/actuator properties and shell modes. (These three actuation components are evaluated next.) In this way, the total control effect $\tilde{F}^c_{mn}$ introduced by the multi-DOF actuator can be defined as

$$\tilde{F}^c_{mn} = \tilde{M}_{xmn} + \tilde{N}_{\psi mn} + \tilde{M}_{\psi mn}. \tag{18}$$

Combining these three components of the distributed modal control force related to the photodeformation strain gives

$$\ddot{\eta}_{mn} + 2\xi_{mn}\omega_{mn}\dot{\eta}_{mn} + \omega^2_{mn}\eta_{mn} = F^c_{mn}, \tag{19a}$$

where

$$F^c_{mn} = -\bar{S}(\tilde{M}_{xmn} + \tilde{N}_{\psi mn} + \tilde{M}_{\psi mn}). \tag{19b}$$

Again, the control action is an index for actuation "magnitude" of the microscopic membrane or bending control effects of the photostrictive actuator. The control action is determined by the photodeformation characteristics, actuator and shell dimensions, mode numbers and the actuator location. Comparing these control actions, one can evaluate the modal control effectiveness of the multi-DOF actuator system.

5. Evaluation of actuator effectiveness

In order to evaluate the control effect of this new multi-DOF actuator, comparison between the one-piece mono-axial actuator and the multi-DOF actuator is provided first. In this study, the shell is made of steel and the dimensions, respectively, are $L=0.4$ m, $\psi^*=\pi/3$, $h=0.4\times10^{-3}$ m and $R=L/\psi^*$. Note that the longitudinal length is equal to the circumferential arc length, i.e., the overall shell is nearly "square." The four regions of the multi-DOF PLZT actuator are insulated from each other and also from the shell. Detailed material parameters are provided in Appendix A. Modal actuation effects of the one-piece actuator are discussed first, followed by those of the multi-DOF actuator.

5.1. One-piece actuator

Earlier studies indicate that the most effective arrangement of the photostrictive actuator is to align the polarized direction with the circumferential direction of the cylindrical shell [1,17,18]. Thus, a one-piece square actuator polarized in the circumferential direction is located in the center region of the cylindrical shell structure. Fig. 5 illustrates the actuator location (top view), its polarized direction and its coordinates on the shell. Simplification of the actuation effectiveness is derived next.

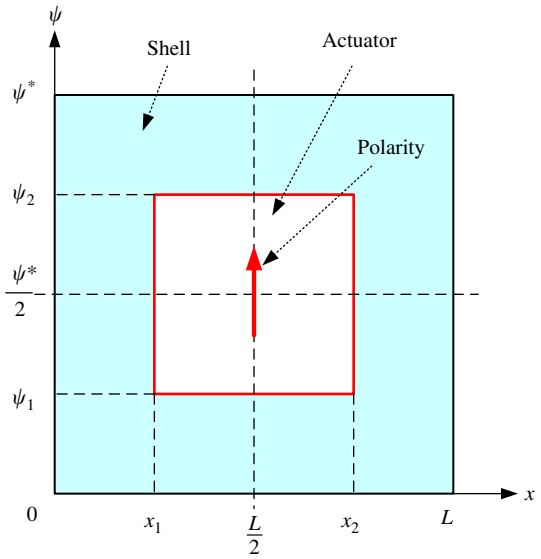

Fig. 5. A shell attached with a one-piece actuator and its location on the shell.

In this case, the control forces/moments in the circumferential direction induced by the photostrictive actuator are

$$N^a_{\psi\psi} = \begin{cases} h^a Y_a \bar{S}, & x_1 \le x \le x_2, \quad \psi_1 \le \psi \le \psi_2, \\ 0 & \text{elsewhere}, \end{cases} \tag{20a}$$

or

$$N^a_{\psi\psi} = h^a Y_a \bar{S}[u_s(x-x_1)-u_s(x-x_2)] \times [u_s(\psi-\psi_1)-u_s(\psi-\psi_2)], \tag{20b}$$

$$M^a_{\psi\psi} = \begin{cases} \dfrac{h+h^a}{2} h^a Y_a \bar{S}, & x_1 \le x \le x_2, \quad \psi_1 \le \psi \le \psi_2, \\ 0 & \text{elsewhere}, \end{cases} \tag{21a}$$

or

$$M^a_{\psi\psi} = \frac{h+h^a}{2} h^a Y_a \bar{S}[u_s(x-x_1)-u_s(x-x_2)] \times [u_s(\psi-\psi_1)-u_s(\psi-\psi_2)]. \tag{21b}$$

Note that there is no control action in the longitudinal direction, because the actuator polarity is aligned with the circumferential axis in this case. The modal control force and its circumferential actuation components are

$$F^c_{mn} = \frac{4}{\rho h L R \psi^*} \int_0^L \int_0^{\psi^*} \left(-\frac{N^a_{\psi\psi}}{R} + \frac{1}{R^2} \frac{\partial^2 M^a_{\psi\psi}}{\partial \psi^2} \right) U_{mn}(x,\psi) R \, dx \, d\psi. \tag{22}$$

And the two circumferential control actions imposed on the shell are

$$\frac{4}{\rho h L R \psi^*} \int_0^L \int_0^{\psi^*} \frac{N^a_{\psi\psi}}{R} U_{mn}(x,\psi) R \, dx \, d\psi = \frac{4h^a}{\rho h L R^2 \psi^*} Y_a \bar{S} \int_0^L \int_0^{\psi^*} \{[u_s(x-x_1)-u_s(x-x_2)] \times [u_s(\psi-\psi_1)$$
$$-u_s(\psi-\psi_2)]\} U_{mn}(x,\psi) R \, dx \, d\psi = \frac{4h^a}{\rho h L R \psi^*} Y_a \bar{S} \frac{L\psi^*}{mn\pi^2} \left[\left(\cos\frac{m\pi x_1}{L} - \cos\frac{m\pi x_2}{L} \right) \times \left(\cos\frac{n\pi\psi_1}{\psi^*} - \cos\frac{n\pi\psi_2}{\psi^*} \right) \right] = \tilde{N}_{\psi mn} \bar{S}; \tag{23a}$$

$$\frac{4}{\rho h L R \psi^*} \int_0^L \int_0^{\psi^*} \frac{1}{R^2} \frac{\partial^2 M^a_{\psi\psi}}{\partial \psi^2} U_{mn}(x,\psi) R \, dx \, d\psi = \frac{2(h+h^a)h^a}{\rho h L R^3 \psi^*} Y_a \bar{S} \int_0^L \int_0^{\psi^*} \frac{\partial^2}{\partial \psi^2} \{[u_s(x-x_1)-u_s(x-x_2)] \times [u_s(\psi-\psi_1)-u_s(\psi-\psi_2)]\}$$
$$\times U_{mn}(x,\psi) R \, dx \, d\psi = \frac{-2(h+h^a)h^a}{\rho h L R^2 \psi^*} Y_a \bar{S} \frac{nL}{m\psi^*} \left[\left(\cos\frac{m\pi x_1}{L} - \cos\frac{m\pi x_2}{L} \right) \times \left(\cos\frac{n\pi\psi_1}{\psi^*} - \cos\frac{n\pi\psi_2}{\psi^*} \right) \right] = -\tilde{M}_{\psi mn} \bar{S}. \tag{23b}$$

As discussed previously, the distributed modal control force becomes

$$F^c_{mn} = -(\tilde{N}_{\psi mn} + \tilde{M}_{\psi mn}) \bar{S}. \tag{24}$$

Thus, the total control action is defined as

$$\tilde{F}^c_{mn} = \tilde{N}_{\psi mn} + \tilde{M}_{\psi mn}. \tag{25}$$

Furthermore, the actuator size is also evaluated and it is defined by the length ratio $\Delta = L^a/L$ = actuator length/shell length. Note that $\Delta = L^a/L = 1/2$ implies that the actuator area is 1/4 of the shell area. Four kinds of actuator/shell length ratios are investigated and they are 1/2, 3/4, 7/8 and 1. The total control actions of the four cases related to the shell modes are summarized in Table 1.

Table 1
Control actions of the single one-piece actuator.

Mode	Δ			
	1/2	**3/4**	**7/8**	**1**
(1,1)	4.3102E6	7.3579E6	8.2923E6	8.6204E6
(1,2)	0	0	0	0
(1,3)	−1.5040E6	1.0635E6	2.4531E6	3.0081E6
(2,1)	0	0	0	0
(2,2)	0	0	0	0
(2,3)	0	0	0	0
(3,1)	−1.4367E6	1.0159E6	2.3433E6	2.8735E6
(3,2)	0	0	0	0
(3,3)	5.0134E5	1.4684E5	6.9320E5	1.0027E6

This table suggests that the single one-piece actuator only exhibits control effects to the odd modes and no effect to even ones. Since the actuator is center-located, the symmetrical modes, such as (1,1), (1,3), (3,3), etc., are effectively controlled. But the anti-symmetrical modes, such as (2,2), (2,4), etc., are not controllable, because the positive and negative control actions are counteracted each other. Control effectiveness of the multi-DOF actuator to the cylindrical shell is discussed next.

5.2. Multi-DOF actuator

Recall that the actuation mechanism and the control forces/moments of the multi-DOF actuator were discussed previously. The actuator regions are, respectively, defined by their four corner coordinates. The cylindrical shell with the multi-DOF actuator (top view) is shown in Fig. 6. It is assumed that a high-energy light uniformly irradiates on these four photostrictive segments.

Again, the total modal-dependent actuations of the shell with four length ratios or four actuator sizes, i.e., 1/2, 3/4, 7/8 and 1, are calculated and summarized in Table 2. From Table 2, one can observe that the multi-DOF actuator can control more shell modes, as compared with the one-piece actuator. It also exhibits control effects to even shell modes, such as mode (2,2). However, the shell modes (1,2), (2,1), (2,3) and (3,2), are still uncontrollable, the same as the one-piece actuator. Furthermore, note that the total actuation magnitudes induced by the one-piece actuator are usually larger than those induced by the multi-DOF actuator. This is because the effective actuator axis of the one-piece actuator is aligned with the circumferential axis of the shell and thus it induces the maximal actuations [17,18]. There is only 50 percent of the effective area in the multi-DOF actuator aligned with the most effective circumferential direction of the shell. Accordingly, the actuation magnitudes are roughly 50 percent of those in the one-piece actuator case, except the (2,2) mode.

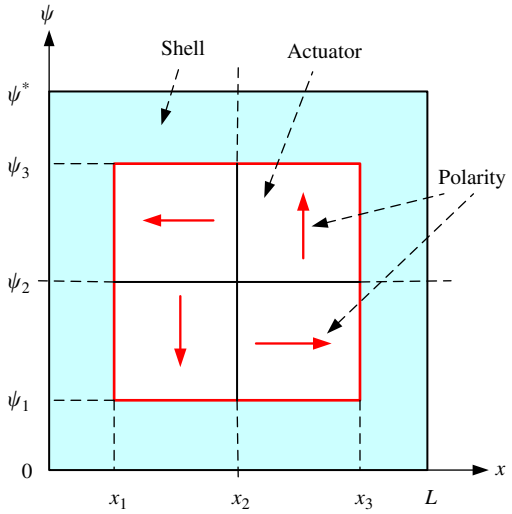

Fig. 6. A shell attached with the multi-DOF actuator and its location to the shell.

Table 2
Control actions of the multi-DOF actuator.

Mode	Δ			
	1/2	**3/4**	**7/8**	**1**
(1,1)	2.1677E6	3.7005E6	4.1704E6	4.3354E6
(1,2)	0	0	0	0
(1,3)	−7.5622E5	5.3473E5	1.2334E6	1.5124E6
(2,1)	0	0	0	0
(2,2)	1.0712E6	3.1218E6	3.9650E6	4.2849E6
(2,3)	0	0	0	0
(3,1)	−7.5622E5	5.3473E5	1.2334E6	1.5124E6
(3,2)	0	0	0	0
(3,3)	2.6329E5	7.7117E4	3.6405E5	5.2659E5

It can be seen that in the even modes, the two corresponding regions of the multi-DOF actuator have a positive control effect on the shell. As to the mode composed of even and odd wave numbers, the actuator has a positive control effect in one region, but a negative one (or amplification) in the other corresponding symmetrical region. Thus, the actuator has no effect on the shell as a whole. It also can be found that the multi-DOF actuator has the same control actions in the (1,3) and (3,1) modes. Although the above two tables summarize specific modal control actuations, the most effective actuator size and curvature do not show clearly. Thus, modal actuations with respect to actuator sizes or curvature are studied next.

5.3. Actuator sizes

Actuation effects concerning various actuator sizes are evaluated to estimate an optimal actuator size in cylindrical shell applications. Since the fundamental mode is generally the most critical mode, control actions of the (1,1) mode of the one-piece actuator and the multi-DOF actuator are calculated and plotted with respect to the actuator/shell length ratio ($\Delta = L^a/L$) for three shell curvatures (i.e., 60°, 120° and 180°), Figs. 7 and 8.

Comparing Tables 1 and 2, as well as Figs. 7 and 8, indicates that enlarging the actuator size generally enhances the control actions, which show slow take-offs and then sharp increases till about the 80 percent actuator coverage. Actuation

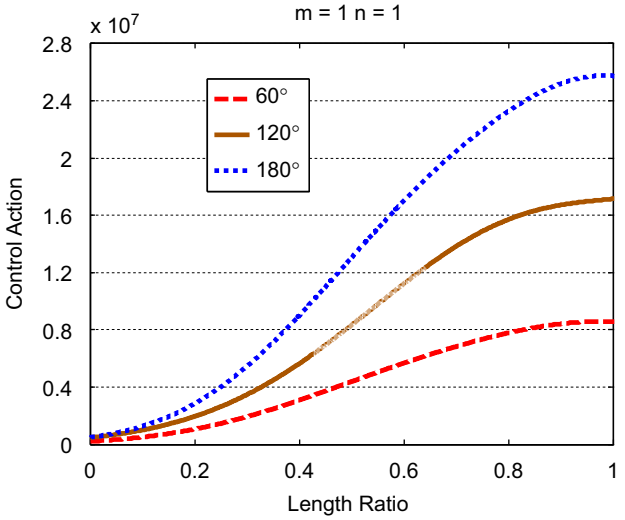

Fig. 7. One-piece actuator control actions to length ratios.

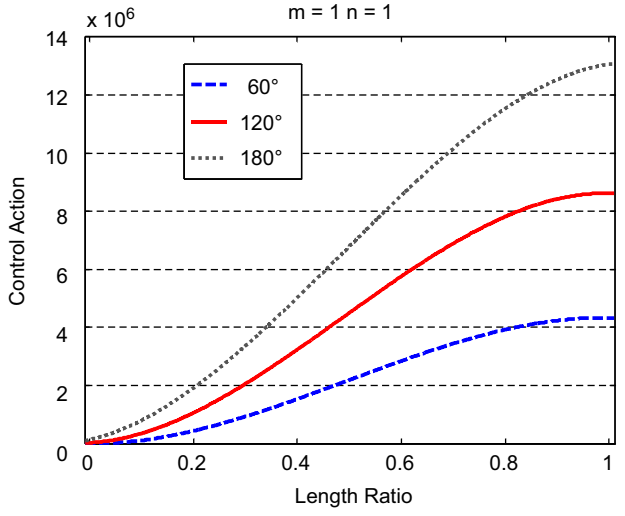

Fig. 8. Multi-DOF actuator control actions to length ratios.

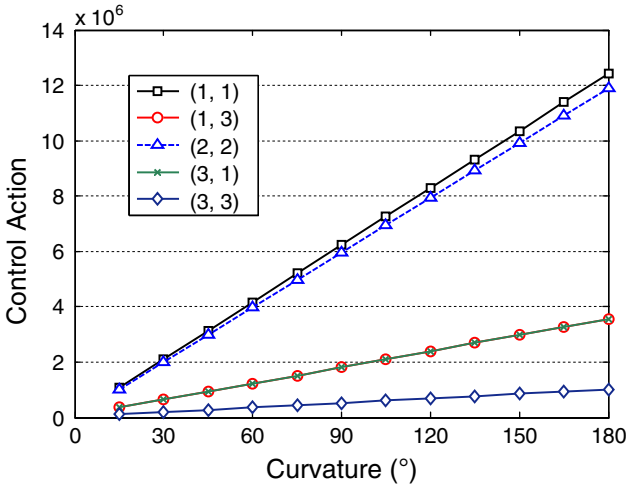

Fig. 9. Multi-DOF actuator control action with respect to the shell curvature.

magnitudes of the one-piece actuator are about double of those of the multi-DOF actuator, since the effective area in the circumferential direction is double. However, when the actuator/shell length ratio reaches around 7/8, the control action is gradually leveling off, i.e., close to that of the fully covered case, in the 60° shell. This "optimal" actuator/shell length ratio (i.e., size) increases as the curvature increases, which implies that larger actuator coverage is needed for deep cylindrical shells. Accordingly, the actuator/shell length ratio of 7/8 is used in the study of curvature effects presented next.

5.4. Shell curvature effects

Earlier analyses suggest that the forces/moments generated by the actuator are functions of shell curvatures. By keeping the actuator and shell areas constant and only changing the shell curvature, one can evaluate the curvature effect to the membrane/bending control actions. Fig. 9 shows the total modal control action of the multi-DOF actuator with respect to the shell curvature change. Since the membrane behavior dominates in deep shells, when the shell curvature increases, so does the membrane control action and the total control action. To the same shell curvature, the control action decreases while the mode number increases. Thus, these data indicate that the multi-DOF actuator works better in deep shells and lower shell modes. Earlier analyses also suggest that the magnitude of control actions remain unchanged if m and n are swapped. Thus, the control actions of the (1,3) and (3,1) modes are the same in Fig. 9.

5.5. Membrane and bending control effects

Analysis suggests that the total modal control force of the multi-DOF actuator is composed of three components, i.e., the circumferential membrane control force, the longitudinal and circumferential bending control moments. Fig. 10 shows the contribution of the bending control to the total control action, i.e., Δ_{bend} (percent), of the shell with respect to various shell curvatures. The contribution of the membrane control is the complement of the bending control, i.e., Δ_{mem} (percent) = 100 percent $-\Delta_{bend}$ (percent).

Fig. 10 suggests that the bending control effect reduces as the shell curvature increases, while the shell size and actuator size (i.e., 7/8) remain identical. The membrane control force domains in the total control action and even more significant in deep shells. At constant shell curvature angle, the bending control moment component increases when the wave number increases. It also can be seen that if the shell curvature becomes zero (i.e., beam/plate type), there is only the bending control moment in the total control action. Furthermore, comparison of the bending control percentages, respectively, contributed by the one-piece actuator and the multi-DOF actuator configurations is summarized in Fig. 11(a) and an enlarged detail in (b).

Note that the one-piece actuator only contributes the circumferential control force and moment. Thus, the bending control ratio in the one-piece actuator only depends on the circumferential wave number "n". Accordingly, the bending control ratios of the (1,1) and (3,1) modes are the same, so are the (1,3) and (3,3) modes in Fig. 11. However, the multi-DOF actuator contributes the longitudinal control moment, together with the circumferential control force and moment. Thus, the bending control ratio of the multi-DOF actuator is larger than that of the one-piece actuator.

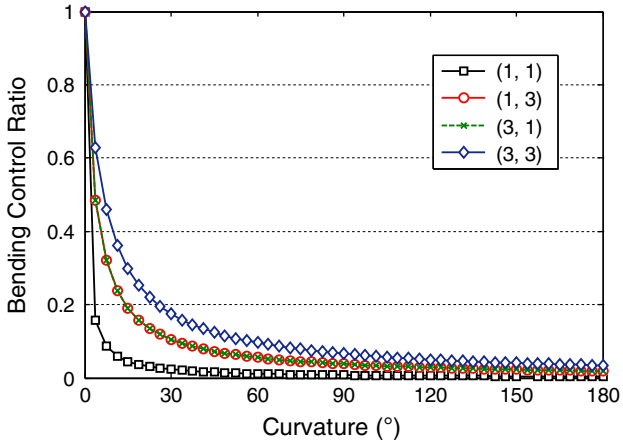

Fig. 10. Bending contribution (percent) of the multi-DOF actuator vs. shell curvature.

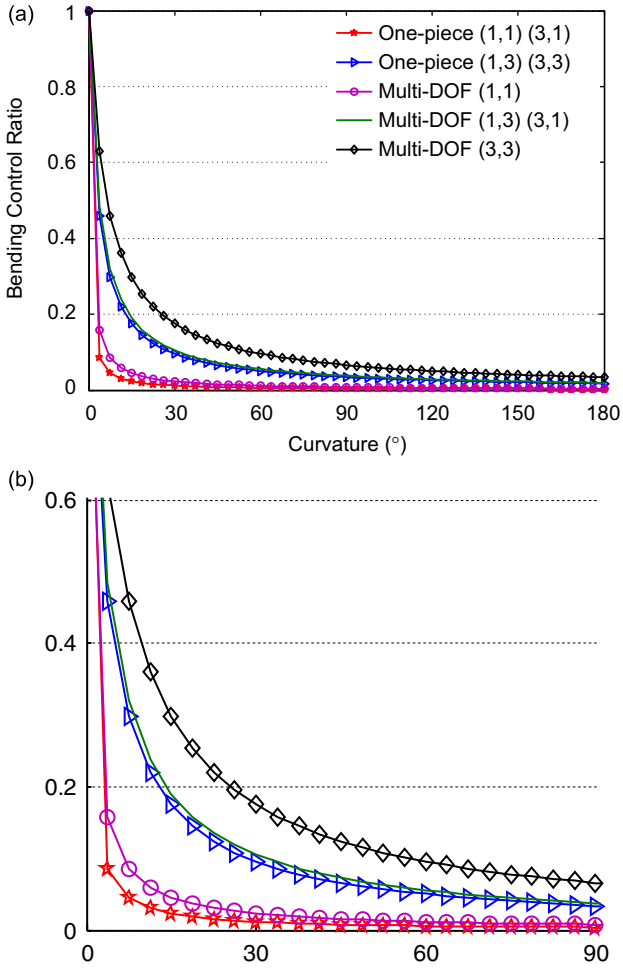

Fig. 11. Comparison of the bending control ratios between the one-piece actuator and the multi-DOF actuator.

6. Conclusions

Non-contact photostrictive actuation is a wireless actuation mechanism that is relatively immured from electromechanical interferences. Since the conventional distributed one-piece actuator only achieves limited modal

control capability, this study focuses on modal control effectiveness of a new multi-DOF actuator design based on four regions of the photostrictive actuators. Mathematical model of the multi-DOF actuator and the shell/actuator coupled system equation were established; control forces/moments and modal control actions were also defined. Actuation effects of a cylindrical shell with the multi-DOF actuator and a single one-piece actuator were studied and compared. Parametric studies of the one-piece actuator and the multi-DOF actuator laminated on the cylindrical shell suggest the following:

(1) The bi-directional multi-DOF actuator can control more shell modes, as compared with the circumferentially laminated single one-piece actuator. However, actuation magnitudes are sometimes less, due to reduced effective actuator coverage in the circumferential direction.
(2) When the actuator/shell length ratio reaches around 7/8, the control action is gradually leveling off, i.e., close to that of the fully covered case, in the 60° shell. This "optimal" actuator/shell length ratio (i.e., size), however, increases as the shell curvature increases. Thus, larger actuator coverage is needed for deep cylindrical shells.
(3) Quantitative comparison indicates that the membrane control force dominates the total shell control action; the bending control moments and the membrane control force are functions of the shell curvature and the mode/wave number. The photostrictive control action exhibits a linear relationship with the shell curvature on the same shell mode. And the actuator is more effective in deep shells or low shell modes.

This study only provides a design guideline of the new multi-DOF actuator, such that an experimental model or physical system can be effectively developed in the near future. Besides, all evaluations of actuation effectiveness are based on uniform lighting to all photostrictive actuators. Irradiating non-uniform and/or non-equal lights to different regions can improve multi-mode controllability of shell structures and distributed precision systems.

Acknowledgments

This research is supported, in part, by a Grant from the National Natural Science Foundation of China (no. 50705017). Prof. Tzou would like to thank HIT's "Ph.D. Supervisor" and the "111 Project" (B07018) programs.

Appendix A

Material properties of steel shell and PLZT are presented in Tables A1 and A2.

Table A1
Material properties of steel shell.

Parameters	Value
Young's modulus Y	$2.1\times10^{10}\,\mathrm{N/m^2}$
Mass density ρ	$7.8\times10^{3}\,\mathrm{kg/m^3}$
Poisson's ratio μ	0.35

Table A2
Material properties of PLZT.

Parameters	Value
Saturated electric field E_s	$2.43\times10^{5}\,\mathrm{V/m}$
Young's modulus Y_a	$6.3\times10^{10}\,\mathrm{N/m^2}$
Actuator thickness h^a	$0.1\times10^{-3}\,\mathrm{m}$
Optical actuator constant α	$0.002772\,\mathrm{m^2/ws}$
Voltage leakage constant β	0.01 V/s
Power of absorbed heat P	$0.23\times10^{3}\,\mathrm{cm^2/s}$
Piezoelectric strain constant	$1.79\times10^{-10}\,\mathrm{m/V}$
Heat capacity H	16 w/°C
Heat transfer rate γ	0.915 w/°Cs
Stress-temperature constant λ	$6.8086\times10^{4}\,\mathrm{N/m^2{\circ}C}$
Pyroelectric constant P_n	$0.25\times10^{-4}\,\mathrm{C/m^2{\circ}C}$
Electric permittivity ε	$1.65\times10^{-8}\,\mathrm{F/m}$

References

[1] H.S. Tzou, *Piezoelectric Shells (Distributed Sensing and Control of Continua)*, Kluwer Academic Publishers, Dordrecht, Boston, London0-7923-2186-3, 1993.
[2] H.S. Tzou, G.L. Anderson (Eds.), *Intelligent Structural Systems*, Kluwer Academic Publishers, Dordrecht, Boston, 1992.
[3] H.S. Tzou, L.A. Bergman (Eds.), *Dynamics and Control of Distributed Parameter Systems*, Cambridge University Press, New York, NY, 1998.
[4] P.S. Brody, Optomechanical bimorph actuator, *Ferroelectrics* 50 (1983) 27–32.
[5] K. Uchino, Photostrictive actuator, *Proceedings, 1990 IEEE Ultrasonics Symposium*, 1990, pp.721–723.
[6] V.M. Fridkin, *Photoferroelectrics*, Springer Verlag, New York, 1979.
[7] V.M. Fridkin, The intrinsic photovoltaic effect in the crystals without a center of symmetry caused by polarized X-irradiation, *Ferroelectrics* 38 (1981) 943–945.
[8] H.S. Tzou, C.S. Chou, Nonlinear optoelectromechanics and photodeformation of optical actuators, *Journal of Smart Materials and Structures* 5 (1996) 230–235.
[9] J. Suski, D. Largeau, A. Steyer, F.C.M. van de Pol, F.R. Blom, Optically activated $ZnO/SiO_2/Si$ cantilever beams, *Sensors & Actuators* 24 (1990) 221–225.
[10] Y. Morikawa, T. Nakada, D.H. Cao, Estimation of dynamic characteristics of bimorph type optical actuator and proposal of opto-pneumatic servo system, *Journal of Mechanical Engineering Laboratory (Japanese)* 47 (1993) 237–246.
[11] S.Y. Chu, K. Uchino, Photoacoustic devices using PLZT ceramics, *Proceedings, 1994 IEEE International Symposium of Applied Ferroelectrics*, 1994.
[12] T. Fukuda, S. Hattori, F. Arai, H. Matsuura, T. Hiramatsu, Y. Ikeda, A. Maekawa, Characteristics of optical actuator–servomechanisms using bimorph optical piezoelectric actuator, *Proceedings, 1993 IEEE Robotics & Automation Conference*, Atlanta, May 1993, pp. 618–623.
[13] D.C. Sun, L. Tong, Theoretical investigation on wireless vibration control of thin beams using photostrictive actuators, *Journal of Sound and Vibration* 312 (2008) 182–194.
[14] H.H. Yue, Z.Q. Deng, H.S. Tzou, Non-contact precision actuation and optimal actuator placement of hybrid photostrictive beam structure systems, *IDETC2007 Proceeding, DETC2007-34995, 2007.9*, Las, Vegas, Nevada, USA, 2007.
[15] B. Liu, H.S. Tzou, Distributed photostrictive actuation and opto-piezoelectricity applied to vibration control of plates, *ASME Journal of Vibration and Acoustics* 120 (1998) 937–943.
[16] H.R. Shih, H.S. Tzou, M. Saypuri, Structural vibration control using spatially configured opto-electromechanical actuator, *Journal of Sound and Vibration* 284/1–2 (2005) 361–378 (ShlMultiOp5.Opto3).
[17] H.R. Shih, R. Smith, H.S. Tzou, Photonic control of cylindrical shells with electro-optic photostrictive actuators, *AIAA Journal* 42 (2) (2004) 341–347.
[18] H.S. Tzou, Y. Bao, Parametric study of segmented transducers laminated on cylindrical shell part 2: actuator patches, *Journal of Sound and Vibration* 197 (2) (1996) 225–249.
[19] H.R. Shih, H.S. Tzou, Photostrictive actuators for photonic control of shallow spherical shells, *Journal of Smart Materials and Structures* 16 (2007) 1712–1717.
[20] H.H. Yue, G.L. Sun, Z.Q. Deng, H.S. Tzou, A new multi-DOF photostrictive actuator for dynamic control of shells: modeling and analysis, Paper no. IMECE2008-68011, 2008 ASME IMECE, Boston, MA, October 31–November 06, 2008.